

Relaxed Rotational Equivariance via G -Biases in Vision

Zhiqiang Wu¹, Licheng Sun¹, Yingjie Liu¹, Jian Yang³, Hanlin Dong¹, Shing-Ho J. Lin⁴, Xuan Tang², Jinpeng Mi⁵, Bo Jin¹, Xian Wei^{1†}

¹Software Engineering Institute, East China Normal University

²School of Communication and Electronic Engineering, East China Normal University

³School of Geospatial Information, Information Engineering University

⁴School of Engineering, Hong Kong University of Science and Technology

⁵Institute of Machine Intelligence, University of Shanghai for Science and Technology

Abstract

Group Equivariant Convolution (GConv) can effectively handle rotational symmetry data. They assume uniform and strict rotational symmetry across all features, as the transformations under the specific group. However, real-world data rarely conforms to strict rotational symmetry commonly referred to as Rotational Symmetry-Breaking in the system or dataset, making GConv unable to adapt effectively to this phenomenon. Motivated by this, we propose a simple but highly effective method to address this problem, which utilizes a set of learnable biases called the G -Biases under the group order to break strict group constraints and achieve **Relaxed Rotational Equivariant Convolution** (RREConv). We conduct extensive experiments to validate Relaxed Rotational Equivariance on rotational symmetry groups C_n (e.g. C_2 , C_4 , and C_6 groups). Further experiments demonstrate that our proposed RREConv-based methods achieve excellent performance, compared to existing GConv-based methods in classification and detection tasks on natural image datasets.

Introduction

Symmetry prior such as equivariance plays a vital role in deep learning (Bogatskiy et al. 2022; He et al. 2021; Esteves 2020; Ravanbakhsh, Schneider, and Poczos 2017). Given the assumption of perfect symmetry in data, recent works on equivariant networks are constrained to operate as strict equivariant or invariant functions. They have been shown to learn inherent symmetry information without additional data, achieving excellent results with improved efficiency and generalization ability (Cohen and Welling 2016a,b; Kondor and Trivedi 2018; Ghosh et al. 2022; Kaba et al. 2023; Kaba and Ravanbakhsh 2024).

However, real-world physical systems seldom adhere to perfect symmetry due to the influence of external factors, a phenomenon commonly termed Symmetry-Breaking (Wang, Walters, and Yu 2022; Barone and Theophilou 2008; Wang et al. 2024; Vernizzi and Wheater 2002; Ghosh et al. 2022; Kaba and Ravanbakhsh 2024). We observed Symmetry-Breaking occurrences within the visual domain. A common example can be seen in Figure 1. In (a), a car turns by 90 degrees, which can be challenging to achieve precisely in practical situations. Conversely, in (b), a car

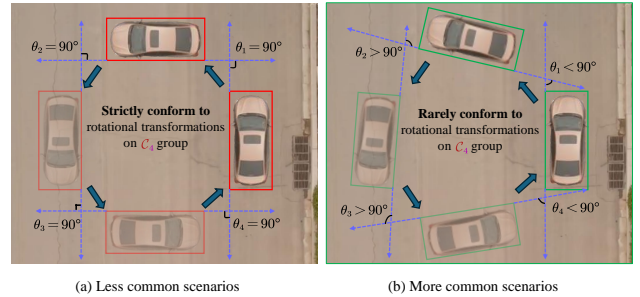


Figure 1: A car turning right at an angle not exactly 90 degrees represents a deviation from rotational symmetry on the group C_4 , leading to rotational Symmetry-Breaking.

turns by less than 90 degrees, often with a slightly randomized angle change, reflecting a more realistic depiction of a car's turning motion in real-world settings. Strict rotational symmetry constraints significantly impede equivariant networks from accurately modeling real-world physical scenarios and performing visual perception.

In this paper, we mainly focus on rotational symmetry and explore the rotational Symmetry-Breaking based on GConv (Cohen and Welling 2016a) on the rotation group C_n in computer vision. Therefore, by rethinking the construction process and principles of GConv, we found that under strict group G transformations (G -transformations), each G -transformation convolution filter shares the same copy value, differing only in their positions. This is the key to GConv's strict equivariance. For example, in the C_4 group, GConv cannot effectively model objects or scenes with rotations other than 90, 180, and 270 degrees. Therefore, we focus on how to relax the strict G -transformation convolution filter value-sharing problem to adapt to rotational Symmetry-Breaking.

Inspired by convolution biases, we introduce a set of learnable biases under the group order to add to the G transformation convolution filter. We referred to these biases as G -Biases, and these GConv on the rotation groups C_4 with G -Biases as **Relaxed Rotational Equivariant Convolution** (RREConv). The rotational equivariance of GConv is called **Strict Rotational Equivariance** (SRE), and for RREConv, it

† Corresponding author: Xian Wei (xwei@tum.de).

is called **Relaxed Rotational Equivariance (RRE)** in our paper. The difference between GConv and RREConv filters can be seen in Figure 2. In the Experiments section, the ablation experiments prove that our RREConv achieved excellent results with a small parameter increase compared to GConv.

The main contributions are as follows:

- To the best of our knowledge, we are the first to explore rotational symmetry-breaking situations in vision.
- We propose a simple yet efficient method to address rotational symmetry-breaking based on the existing GConv.
- Our proposed RREConv, which has fewer parameters, not only increases performance but also achieves excellent results and can be used as a plug-and-play module with different models.

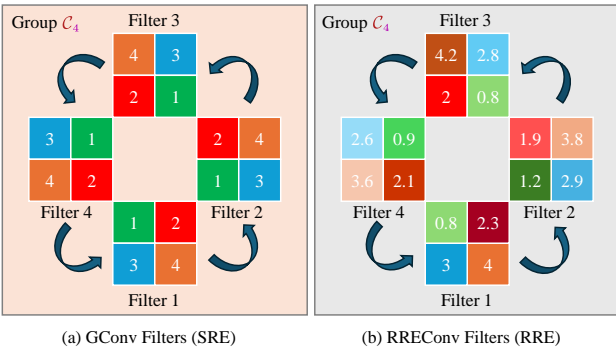


Figure 2: The filters between Strict Rotational Equivariance (SRE) and Relaxed Rotational Equivariance (RRE) on the rotation group C_4 . Filters 1-4 in (a) have the same values in all four directions, whereas Filters 1-4 in (b) have slightly different values in four directions.

Related works

Strict Rotational Equivariance (SRE). Strict Rotational Equivariance is critical for neural networks handling rotated data, especially in computer vision tasks involving 2D images and 3D objects (Marcos, Volpi, and Tuia 2016). As demonstrated by the pioneering work (Cohen and Welling 2016a), introducing group equivariance into traditional CNNs led to the development of novel G-CNNs. Foundational networks such as (Li et al. 2018; Marcos et al. 2017; Chidester, Do, and Ma 2018; Weiler and Cesa 2021), have achieved notable success in exploring the rotational equivariance of images. In (Veeling et al. 2018; Müller et al. 2021), the application of rotational equivariance in medicine has achieved excellent performance due to the frequent presence of rotational equivariance in medical data. Moreover, rotational equivariance is also prevalent in 2D object detection. For instance, ReDet (Han et al. 2021) introduces rotational equivariance into aerial object detection. MORE-Net (Zhu et al. 2022) proposes the multi-oriented ground objects detector to extract rotation-invariant semantic representations. In addition, EquiSym (Seo et al. 2022) outputs group

equivariant score maps for rotational centers through end-to-end rotational equivariant feature maps. Rotational equivariance has also seen significant advancements in 3D vision. In (Weiler et al. 2018; Fuchs et al. 2020), 3D Steerable CNNs and SE(3)-Transformers were proposed to explore 3D rotational equivariance. In 3D object detection, 3D equivariance remains crucial. DuEqNet (Wang et al. 2023) focuses on introducing 3D rotation group equivariance constraints in 3D object detection tasks, highlighting the importance of rotational equivariant features in enhancing the robustness of 3D detection models. ProEqBEV (Liu et al. 2024) demonstrates the effectiveness of rotational equivariant BEV features. These methods preserve the structural integrity of learned features under rotation, enhancing the robustness of the network to such strict rotational transformations.

Relaxed Rotational Equivariance (RRE). However, the methods of SRE mentioned above make them poorly suited for handling rotational Symmetry-Breaking in both 2D and 3D fields, as they assume that the data exhibits perfect rotational symmetry, which is rarely the case in real-world scenarios (Wu, Hu, and Kong 2015; Dieleman, De Fauw, and Kavukcuoglu 2016; Kavukcuoglu et al. 2009). In contrast, explorations into RRE reveal a significant gap in the current research. While SRE models are effective under ideal conditions, they fall short when dealing with the more common, imperfect symmetries in the real world. In some theoretical works (Kaba and Ravanbakhsh 2024; Kaba et al. 2023), they meticulously analyze the importance and potential application scenarios of relaxed equivariance. Partial rotational equivariance, as highlighted in (Romero and Lohit 2023), is more effective for representing real-world data compared to full rotational equivariance. Similarly, (van der Ouderaa, Romero, and van der Wilk 2022) emphasizes that equivariance constraints can be overly restrictive. (Wang et al. 2024) explores the relaxed equivariance of physical systems. These methods confirm that relaxed equivariance (e.g., especially RRE) is more suitable for real-world scenarios.

Rotational Symmetry and Symmetry-Breaking. Rotational symmetry (Li, Nagano, and Terashi 2024), a fundamental concept in natural systems, pertains to objects or patterns that retain their appearance when rotated by specific angles (Barone and Theophilou 2008). Though prevalent in theoretical models, this pristine form of symmetry is often disrupted in real-world scenarios, a phenomenon referred to as rotational Symmetry-Breaking (Vernizzi and Wheater 2002). Recent progress in understanding these deviations has spurred the creation of new methodologies aimed at tackling Symmetry-Breaking challenges. For instance, methodologies suggested by (Desai, Nachman, and Thaler 2022) propose techniques to integrate Symmetry-Breaking elements into models, enhancing their performance in tasks such as data mining and analysis. However, most researchers focus on rotational symmetry and often overlook the phenomenon of rotational Symmetry-Breaking. Therefore, this paper primarily focuses on addressing the phenomenon of rotational Symmetry-Breaking.

Preliminary

Definition of Strict Equivariance. Assume that an input group representation φ_X of G acts on X and an output group representation φ_Y of G acts on Y . A learnable function $f_{\text{strict}} : X \rightarrow Y$ is *Strict Equivariant* if

$$f_{\text{strict}}(\varphi_X(g)(\mathbf{x})) = \varphi_Y(g)f_{\text{strict}}(\mathbf{x}), \quad (1)$$

where all $\mathbf{x} \in X$ and $g \in G$.

Definition of ε -Relaxed Equivariance. Consistent with the above definition, a learnable function $f_{\text{relaxed}} : X \rightarrow Y$ is *Relaxed Equivariant* if

$$\| f_{\text{relaxed}}(\varphi_X(g)(\mathbf{x})) - \varphi_Y(g)f_{\text{relaxed}}(\mathbf{x}) \| \leq \varepsilon, \quad (2)$$

where all $\mathbf{x} \in X$ and $g \in G$. The upper bound ε is usually a small number, with a relatively large value indicating a greater level of relaxation, and a relatively small value indicating a smaller level of relaxation (or a stronger level of equivariance). Especially when ε is 0, $f_{\text{relaxed}} = f_{\text{strict}}$. Note that ε is determined by the level of Symmetry-Breaking of the dataset (or system), which is an implicit constant.

Strict Equivariant Network. Given a set of strict equivariant functions $\{f_i\}$, a strict equivariant network can be the composition function of $\{f_i\}$. Assume f_1 and f_2 satisfy strict equivariance and $g_1, g_2 \in G$, then their composition $f_1 \circ f_2 = f_1(f_2(\dots))$ also satisfies strict equivariance. Since $f_1(g_1 \cdot x) = g_1 \cdot f_1(x)$ and $f_2(g_2 \cdot x) = g_2 \cdot f_2(x)$, we have $f_2(f_1(g_1 \cdot x)) = f_2(g_1 \cdot f_1(x)) = g_1 \cdot f_2(f_1(x))$, completing the proof. The challenge of a strict equivariant network is in designing equivariant layers. Two typical methods are raised by weight sharing (Cohen and Welling 2016a) and weight tying (Cohen and Welling 2016b).

Relaxed Equivariant Network. A strict equivariant network considers equivariance but simply assumes uniform strict equivariance across all features. However, real-world data rarely conforms to strict equivariance. To address this problem, we can relax the G -transformation filters to realize relaxed equivariance. Also like above, given a set of relaxed equivariant functions $\{\tilde{f}_i\}$, a relaxed equivariant network can be the composition function of $\{\tilde{f}_i\}$. The proof can be referred to (Kaba and Ravanbakhsh 2024).

Group Equivariant Convolution

Group Equivariant Convolution (GConv) achieves equivariant inductive bias by sharing weights through convolution filters under group transformations. In a special case, CNNs achieve translational equivariance through translational transformations on the plane \mathbb{Z}^2 .

In the beginning, define a group operator $\Phi^G(\circ)$ performs the G -transformations in the last two dimensions and cyclical permutations in the input channel dimension for \circ , and the symbol $[\dots]$ denotes the Pytorch style index operation. For convenience, we also define C_l , k_l , h_l , and w_l denote the channel number, kernel (or filter) size, width, and height of the 2D input (or the output) in the l -layer, respectively. These definitions are used in the following text.

Regular Convolution. Assume the input \mathcal{Y}_l of size $[C_l, h_l, w_l]$ on the plane \mathbb{Z}^2 , and the convolution filter $\mathcal{F}_l^{\mathbb{Z}^2}$ of size $[C_{l+1}, C_l, k_l, k_l]$. For all $u \in [1, C_{l+1}]$, a regular convolution in the l -layer can be performed by convolving over the input channel C_l and summing up the outputs as follows:

$$\mathcal{Y}_{l+1}[u, :, :] = \sum_m^{C_l} \mathcal{Y}_l[m, :, :] * \mathcal{F}_l^{\mathbb{Z}^2}[u, m, :, :], \quad (3)$$

with the size of \mathcal{Y}_{l+1} is $[C_{l+1}, h_{l+1}, w_{l+1}]$, in which C_{l+1} , h_{l+1} and w_{l+1} denote the output channel number, height and width in the l -layer (or the input channel number, height and width in the $\{l+1\}$ -layer), respectively. And the operator $*$ denotes convolution operation.

Lift Convolution. The first layer of G-CNNs typically lifts the input on the plane \mathbb{Z}^2 to the group G . Assume the input \mathcal{Y}_1 of size $[C_1, h_1, w_1]$ and the initial weight $\mathcal{W}_1^{\mathbb{Z}^2}$ with Kaiming distribution of size $[C_2, C_1, k_1, k_1]$ on the plane \mathbb{Z}^2 in the first layer. Therefore, we obtain the full lift convolution filter $\mathcal{F}_1^G = \Phi^G(\mathcal{W}_1^{\mathbb{Z}^2})$ of size $[C_2, G_2, C_1, k_1, k_1]$ that contains an additional dimension G_2 for the output group. Note that \mathcal{F}_1^G is constructed from $\mathcal{W}_1^{\mathbb{Z}^2}$ during each forward function. For all $u \in [1, C_2]$, $v \in [1, G_2]$, a lift convolution can be performed by convolving over the input channel C_1 and summing up the outputs as follows:

$$\mathcal{Y}_2[u, v, :, :] = \sum_m^{C_1} \mathcal{Y}_1[m, :, :] * \mathcal{F}_1^G[u, v, m, :, :], \quad (4)$$

with the size of the output \mathcal{Y}_2 is $[C_2, G_2, h_2, w_2]$.

Group Convolution. Unlike the input on the plane \mathbb{Z}^2 , GConv typically encodes the added group G in an extra tensor dimension. Therefore, assume the input \mathcal{Y}_l of size $[C_l, G_l, h, w]$ on the group G , where G_l denotes the dimension of G in the l -layer ($l \geq 2$), and the initial weight \mathcal{W}_l^G with Kaiming distribution of size $[C_{l+1}, C_l, G_l, k_l, k_l]$ contains an additional dimension G_l for the input group. Then, we obtain the full group convolution filter $\mathcal{F}_l^G = \Phi^G(\mathcal{W}_l^G)$ of size $[C_{l+1}, G_{l+1}, C_l, G_l, k_l, k_l]$ containing an additional dimension G_{l+1} for the output group. For all $u \in [1, C_{l+1}]$, $v \in [1, G_{l+1}]$, a group convolution can be performed by convolving over the input channel C_l and input group dimension G_l , and summing up the outputs as follows:

$$\mathcal{Y}_{l+1}[u, v, :, :] = \sum_m^{C_l} \sum_n^{G_l} \mathcal{Y}_l[m, n, :, :] * \mathcal{F}_l^G[u, v, m, n, :, :], \quad (5)$$

with the size of the output \mathcal{Y}_{l+1} is $[C_{l+1}, G_{l+1}, h_{l+1}, w_{l+1}]$. Since the group convolution is the function $f : G \rightarrow G$, we have $G_{l+1} = G_l = \text{Dim}(G)$, where $\text{Dim}(G)$ is the dimensions of G (e.g, 2 on \mathcal{C}_2 , 4 on \mathcal{C}_4 , and 8 on \mathcal{C}_8).

The Proposed Method

This paper focuses on a specific case: Relaxed Rotational Equivariance (RRE) for rotational Symmetry-Breaking on the rotation group \mathcal{C}_n . Then we introduce the method of

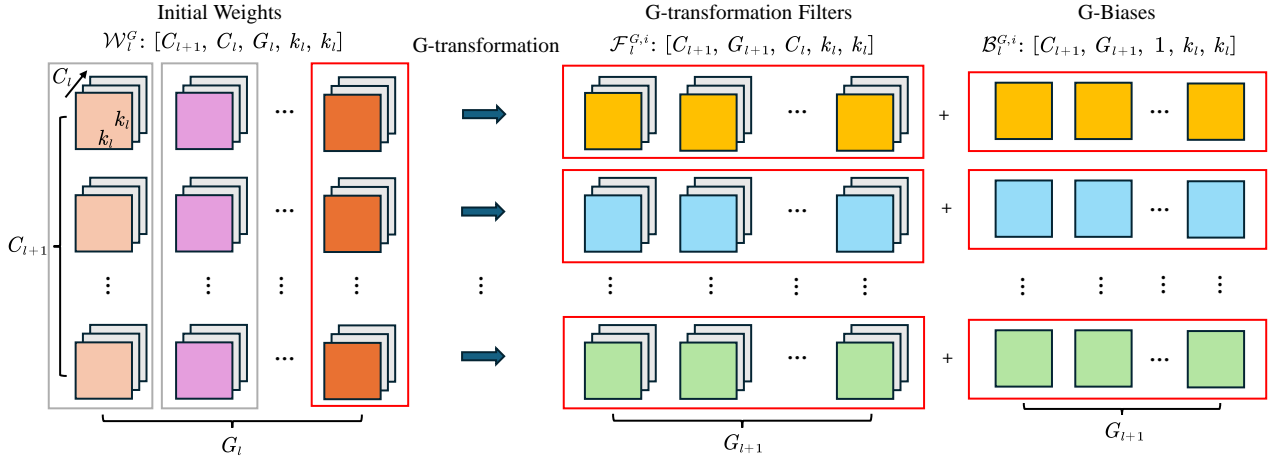


Figure 3: The construction of RREF. Note that the initial filter has G_l columns, and only the G -transformation in the last column (**Red Box**) is shown in the figure. The operations in the remaining columns (**Gray Box**) are the same.

our proposed **Relaxed Rotational Equivariant Convolution** (RREConv), and the model architecture for both classification and detection tasks based on RREConv in 2D vision.

Relaxed Rotational Equivariant Filter

The construction of the Relaxed Rotational Equivariant Filter (RREF) is the key to our method. Assume an initial weight \mathcal{W}_l^G of size $[C_{l+1}, C_l, G_l, k_l, k_l]$ with Kaiming distribution on the group G in the l -layer, where $G = \mathcal{C}_n$, and $G_l = n$ for our RRE especially. Define a set of affine matrices $\mathcal{A} = \{\mathcal{A}_i \mid i \in \{0, 1, \dots, n-1\}\}$ for the G -transformation, where

$$\mathcal{A}_i = \begin{bmatrix} \cos(2\pi i/n) & -\sin(2\pi i/n) \\ \sin(2\pi i/n) & \cos(2\pi i/n) \end{bmatrix}. \quad (6)$$

Before G -transformation for coordinates, assume the coordinate system is at the center of 2D plane, and define a function $\text{CoorSet}(\circ)$ to obtain the set of all coordinates of \circ . For all $u \in [1, C_{l+1}], m \in [1, C_l], n \in [1, G_l]$, 2D coordinate pair $(\mathbf{x}, \mathbf{y}) \in \text{CoorSet}(\mathcal{W}_l^G[u, m, n, :, :])$, we can obtain new 2D coordinate pair $(\tilde{\mathbf{x}}, \tilde{\mathbf{y}})$ after G -transformation for coordinates on \mathcal{W}_l^G as follows:

$$(\tilde{\mathbf{x}}_i, \tilde{\mathbf{y}}_i)^\top = \mathcal{A}_i (\mathbf{x}, \mathbf{y})^\top, \quad \forall i \in \{0, 1, \dots, n-1\} \quad (7)$$

Now, we can obtain the strict rotational equivariant i -filter at group order i on G as follows:

$$\mathcal{F}_l^{G,i}[u, m, n, \tilde{\mathbf{x}}_i, \tilde{\mathbf{y}}_i] = \mathcal{W}_l^G[u, m, n, \mathbf{x}, \mathbf{y}], \quad (8)$$

if $(\tilde{\mathbf{x}}_i, \tilde{\mathbf{y}}_i) \in \text{CoorSet}(\mathcal{F}_l^{G,i}[u, m, n, :, :])$. Note that some out-of-bounds coordinates of $\mathcal{F}_l^{G,i}$ may occur in some groups (e.g. \mathcal{C}_6 , and \mathcal{C}_8) except \mathcal{C}_2 and \mathcal{C}_4 . Based on this reason, some coordinates remain unassigned after the G -transformation from \mathcal{W}_l^G . For these coordinates, we employ *Bilinear Interpolation*. For our RREF, we introduce a set of learnable G -biases $\mathcal{B}_l^G = \{\mathcal{B}_l^{G,i} \mid i \in \{0, 1, \dots, n-1\}\}$, where the size of $\mathcal{B}_l^{G,i}$ is $[C_{l+1}, 1, 1, k_l, k_l]$, with Zero distribution in the l -layer. Note that \mathcal{B}_l^G can be updated end-to-end

during the training period to adapt the Symmetry-Breaking in the dataset. Therefore, the final values of \mathcal{B}_l^G in l -layer are determined by datasets. Then, the relaxed rotational equivariant i -filter at group order i on G as follows:

$$\mathcal{R}_l^{G,i}[u, m, n, :, :] = \mathcal{F}_l^{G,i}[u, m, n, :, :] + \mathcal{B}_l^{G,i}[u, 1, 1, :, :]. \quad (9)$$

Thus, the full RREF in the l -layer can be stacked as follows:

$$\mathcal{R}_l^G = \text{Stack}(\{\mathcal{R}_l^{G,i} \mid i \in \{0, 1, \dots, n-1\}\}), \quad (10)$$

with the size of $[C_{l+1}, G_{l+1}, C_l, G_l, k_l, k_l]$. An easily understandable construction of the RREF can be seen in Figure 3.

Relaxed Rotational Lift Convolution

Assume the input \mathcal{X}_1 of size $[C_1, h_1, w_1]$ on the plane \mathbb{Z}^2 in the first layer. Similar to the lift convolution in equation (4), for all $u \in [1, C_2]$, Relaxed Rotational Lift Convolution (RRLConv) can be performed by convolving over the input channel C_1 , and summing up the outputs as follows:

$$\mathcal{X}_2[u, v, :, :] = \sum_m^{C_1} \mathcal{X}_1[m, :, :] * \mathcal{R}_1^G[u, v, m, :, :]. \quad (11)$$

Note that, the constructions of \mathcal{R}_1^G and \mathcal{R}_l^G for $l \geq 2$ are the same, with \mathcal{R}_1^G being slightly different in that it has no extra input dimension G_1 .

Relaxed Rotational Equivariant Convolution

Also, assume the input \mathcal{X}_l of size $[C_{l+1}, C_l, G_l, h_l, w_l]$ in the l -layer ($l \geq 2$) on the group G , i.e., the group \mathcal{C}_n . Similar to the group convolution in equation (5), for all $u \in [1, C_{l+1}], v \in [1, G_{l+1}]$, RREConv can be performed by convolving over the input channel C_l and the input group dimension G_l , and summing up the outputs as follows:

$$\mathcal{X}_{l+1}[u, v, :, :] = \sum_m^{C_l} \sum_n^{G_l} \mathcal{X}_l[m, n, :, :] * \mathcal{R}_l^G[u, v, m, n, :, :], \quad (12)$$

with the size of $[C_{l+1}, G_{l+1}, C_l, G_l, k_l, k_l]$.

Model Architecture

Based on our RREConv, we propose a **Relaxed Rotational Equivariance Network** (RRENNet). Considering the significant computational and parameter overhead caused by the additional G dimension, we redesign the point-wise and depth-wise versions of our RREConv. We typically adopt the classic structure of ResNet (He et al. 2016), where each PD RREBlock consists of two Point-wise RRECBAs adjusting the input and output channels, with two PD RRECBAs in between, and residual connections are used, as shown in Figure 4. We also propose a **Relaxed Rotational Equivariance Detetor** (RREDet). We use RREDet as a backbone to obtain three scale features in 2-layer, 3-layer, 4-layer, and the FPN+PAN architecture as the neck layer to obtain the final three scale features of size 80×80 , 40×40 , and 20×20 for different-size object detection. Note that, the feature maps in 4-layer are firstly input to the G-SPPF for Spatial Pyramid Pooling (He et al. 2014). Then these features are fed into the G-Max Pooling. Finally, the obtained features are as inputs for the YOLOv8 detector, as shown in Figure 5. Here, the size of the input is 640×640 .

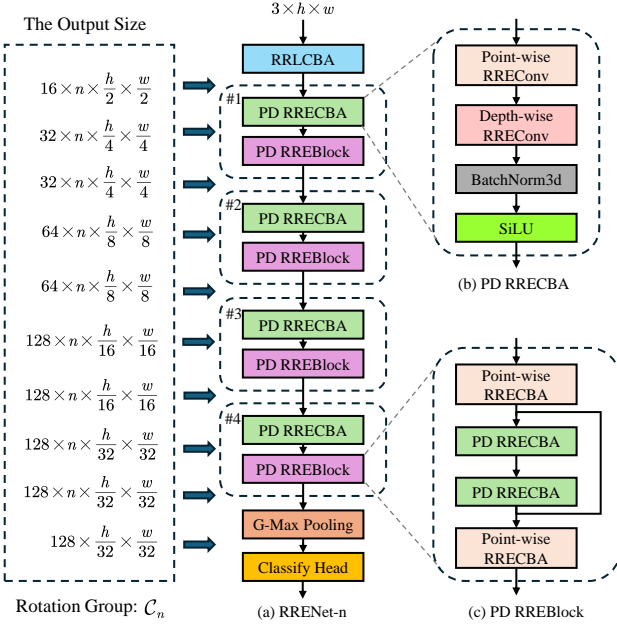


Figure 4: The architecture of our backbone RRENNet-n based on RREConv. Note that n denotes the dimension of C_n , and CBA means Conv + BathNorm + Activate in our paper.

Experiments

In this section, we conduct extensive ablation experiments to demonstrate the effectiveness of our proposed RREConv in both classification and object detection tasks. All the parameters are set the same, and all the experiments are conducted on dual RTX-4090 GPU. We evaluate our method on the CIFAR10 / 100 datasets for the classification tasks, and the PASCAL VOC07+12 and MS COCO 2017 datasets for the

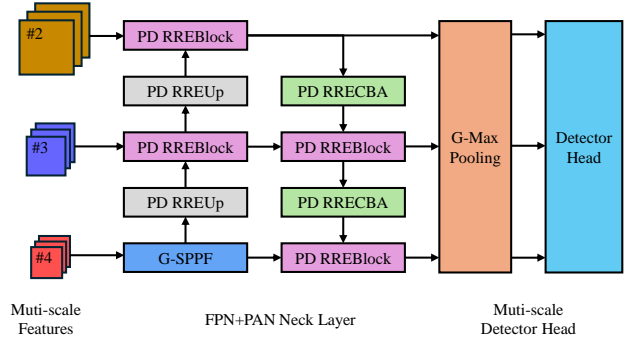


Figure 5: The architecture of our 2D object detector RREDet. Note that #2, #3, and #4 denote features from 2-layer, 3-layer, and 4-layer in our backbone RRENNet, respectively. Note that, the PD RREUp adopts the same structure as the PD RREConv, except for using transposed convolution.

2D object detection tasks. The ablation experiments show that our RRE with small additional parameters compared to SRE, but achieved excellent performance growth.

Datasets

CIFAR10 / 100. The CIFAR-10 dataset consists of 60,000 color images in 10 classes (6000 images per class), with 50,000 for training and 10,000 for testing. CIFAR-100 is similar but with 100 classes (600 images per class) organized into 20 superclasses. We perform classification ablation experiments on these two datasets.

PASCAL VOC07+12. The PASCAL VOC07 dataset has 5,000 training images with annotations for over 12,000 objects. Its successor, VOC12, offers 11,000 training images with annotations for approximately 27,000 objects across 20 object classes. Our ablation experiments focus on the combined VOC 07+12 dataset for 2D object detection.

MS COCO 2017. The MS COCO 2017 dataset comprises 330K images, with annotations for object detection, segmentation, and tracking in 200K images. Spanning 80 categories like cars, animals, and specific items like umbrellas and sports gear, our experiments verify our method's generalizability on this diverse dataset.

Training Details

Data Augmentation. We adopted the same settings as YOLOv8, mainly including Mosaic, Mixup, random perspective, and HSV augmentations.

Parameter Setting. All models are trained for 200 epochs with resized size 224×224 for classification tasks, and 300 epochs with resized size 640×640 for 2D object detection tasks. For both tasks, we use an SGD optimizer with an initial learning rate (lr) of 0.01 and momentum of 0.9.

Experimental Results

Ablation Experiments in Classification. To evaluate the effectiveness of our proposed RREConv, we conduct extensive ablation experiments on the CIFAR10 / 100 datasets,

Table 1: Ablation experiments compared with NRE, SRE, and RRE on the group \mathcal{C}_n ($n = 2, 4, 6, 8$) on the CIFAR10 / 100 test dataset and the PASCAL VOC07+12 test dataset. All models are trained on the architecture of our RRENNet for classification tasks, and our RREDet for 2D object detection tasks.

Group G	Type of Equivariance	CIFAR-10		CIFAR-100		PASCAL VOC07+12		
		Top-1 Acc.	#Param.	Top-1 Acc.	#Param.	AP_{50}^{test}	$AP_{50:95}^{test}$	#Param.
\mathbb{Z}^2	NRE	95.6	1.08M	77.2	1.19M	79.1	58.6	3.11M
\mathcal{C}_2	SRE	94.4 _{base}	0.49M	76.1 _{base}	0.61M	78.9 _{base}	58.3 _{base}	1.81M
	RRE	95.0 _{+0.6}	0.51M	76.6 _{+0.5}	0.63M	80.1 _{+1.2}	59.7 _{+1.4}	1.85M
\mathcal{C}_4	SRE	95.6 _{base}	0.79M	80.1 _{base}	0.91M	83.1 _{base}	64.1 _{base}	2.83M
	RRE	96.5 _{+0.9}	0.83M	80.9 _{+0.8}	0.95M	84.1 _{+1.0}	65.2 _{+1.1}	2.91M
\mathcal{C}_6	SRE	96.0 _{base}	1.09M	80.6 _{base}	1.21M	83.8 _{base}	64.7 _{base}	3.85M
	RRE	96.8 _{+0.8}	1.16M	81.3 _{+0.7}	1.27M	84.5 _{+0.7}	65.5 _{+0.8}	3.98M
\mathcal{C}_8	SRE	96.5 _{base}	1.39M	82.1 _{base}	1.39M	85.2 _{base}	66.6 _{base}	4.88M
	RRE	97.2 _{+0.7}	1.48M	82.7 _{+0.6}	1.48M	86.0 _{+0.8}	67.5 _{+0.9}	5.04M

using the architecture of our RRENNet with Non-Rotational Equivariance (NRE) on the plane \mathbb{Z}^2 , with Strict Rotational Equivariance (SRE) and Relaxed Rotational Equivariance (RRE) the rotation group \mathcal{C}_n . For SRE, we replace all RREConv with GConv. For NRE, we replace all RREConv with regular Conv but remove the Group Pooling block. We keep all other parameters consistent in NRE, SRE, and RRE. The results can be seen in Table 1. From the table, the top-1 accuracy of the model with RRE consistently outperforms their NRE and SRE counterparts on the \mathcal{C}_4 , \mathcal{C}_8 , and \mathcal{C}_6 groups. In the \mathcal{C}_2 group, although the top-1 accuracy of the model with RRE and SRE is lower than the model with NRE, its parameters are only half of the model with NRE. The experimental results demonstrate that compared to SRE, RRE can achieve better results in the classification tasks while maintaining less parameter increase.

Ablation Experiments in 2D Object Detection. We also conduct extensive ablation experiments on the PASCAL VOC07+12 test dataset to validate the effectiveness of our RREConv in 2D object detection tasks, using the standard Average Precision (AP) metric. We typically utilize AP_{50} at an Intersection over Union (IoU) threshold of 0.5, and $AP_{50:95}$ across IoU thresholds ranging from 0.5 to 0.95 as key evaluation metrics. Our RREDet uses RRENNet as the backbone layer and FPN+PAN architecture as the neck layer to obtain three scale features of size 80×80 , 40×40 , and 20×20 for different-size object detection. Then these features are fed into the *Group MaxPooling* block. Finally, the obtained features are as inputs for the YOLOv8 universal detector. The detailed architecture is presented in Figure 5. As shown in Table 1, the AP_{50} and $AP_{50:95}$ of the model with RRE consistently surpasses their NRE and SRE counterparts on all groups. The experimental results prove that our RRE can also achieve better results in the 2D object detection tasks and maintain less parameter increase.

Comparison with other models in Classification. Table 2 presents comparative results of our three different-size

RRENNet models (i.e., RRENNet-n, RRENNet-m, and RRENNet-s) on the group \mathcal{C}_4 against other models, including WideResNet, ResNeXt-29, DenseNet-BC, and Res2NeXt-29, on the CIFAR-100 dataset. From the table, our RRENNet-m (\mathcal{C}_4) model achieves a significant improvement in the top-1 accuracy, with a range of 1.4%-5.5% enhancement over other models, but its parameters are only 24%-34% of others.

Comparison with other models in 2D Object Detection. As shown in Table 3, our three different-size RRENNet models (i.e., RREDet-n, RREDet-m, and RREDet-s) on the group \mathcal{C}_4 mainly compares with the advanced YOLOv8 with three size models (i.e., YOLOv8-n, YOLOv8-s, and YOLOv8-m) on the PASCAL VOC07+12 test dataset. Among them, our RREDet-n (\mathcal{C}_4) achieves approximate AP_{50}^{test} and $AP_{50:95}^{test}$ compared to YOLOv8-m, but its parameters are only 11% of YOLOv8-m. Our RREDet-s and RREDet-m (\mathcal{C}_4) exceeds other models in both AP_{50}^{test} and $AP_{50:95}^{test}$. But our RREDet-s (\mathcal{C}_4) achieves a balance between average precision and parameters.

We also conduct experiments on the larger scale MSCOCO 2017 dataset to test the generalization ability of our RREDet model. We compare our RREDet-n (\mathcal{C}_4) with other YOLO family models of the same scale, as shown in Table 4. From the table, our RREDet-n (\mathcal{C}_4) outperforms the other models mentioned above in $AP_{50:95}^{val}$, but is lower than YOLOv5-s in AP_{50}^{val} . Nevertheless, the parameters of YOLOv5-s are two times that of RREDet-n (\mathcal{C}_4). The latest models YOLOv9-n and YOLOv10-n have approximately 70% of the parameters of our RREDet-n (\mathcal{C}_4), but our RREDet-n (\mathcal{C}_4) improves approximately 5% in $AP_{50:95}^{val}$.

Analysis of experimental results. The above ablation experiment and contrast experiment fully prove the progressiveness of our RRE in vision. The rotational symmetry breaking is common in the real world. Therefore, relaxing SRE to obtain our RRE is an effective way to adapt to rotational Symmetry-Breaking. Since our *G*-Biases are

Table 2: Top-1 Accuracy (%) on the CIFAR-100 test dataset.

Model	Top 1 Acc.	#Param.
WideResNet	79.5	36.5M
ResNeXt-29	82.7	68.1M
DenseNet-BC	82.8	25.6M
Res2NeXt-29	83.2	36.7M
RRENet-n (\mathcal{C}_4)	80.9	0.95M
RRENet-s (\mathcal{C}_4)	83.5	2.97M
RRENet-m (\mathcal{C}_4)	85.0	8.66M

learnable parameters that can update end-to-end during the training period. They are automatically updated based on the distribution characteristics of the natural dataset to adapt to rotational Symmetry-Breaking. In Pytorch, we use `torch.nn.Parameter(...)` to define our G -Biases that can be updated by gradient descent direction. Thus, relaxed rotational equivariant networks can achieve better results compared to traditional strict rotational equivariant networks.

Visualization of SRE and RRE

The visualization of SRE and RRE on the group \mathcal{C}_4 can be seen in Figure 6. From the figure, in (b), we observe that the content inside the red circle remained unchanged after rotation, and the overall image shows the same, which reflects the characteristics of SRE. In (c), we find that there are slight differences in the content inside the white circle after rotation, but the overall image presents similarity, which reflects the characteristics of RRE. The similarity of RRE, rather than uniformity, is more common and largely reflects rotational Symmetry-Breaking of objects in the real world.

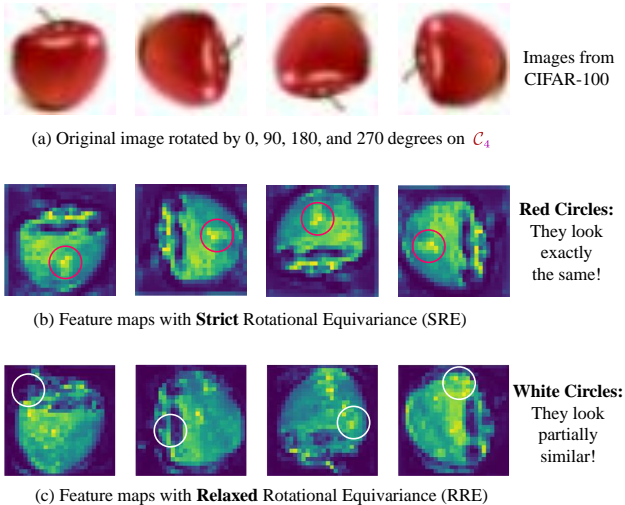


Figure 6: The visualization of SRE and RRE.

Table 3: Average Precise (AP) on the PASCAL VOC07+12 test dataset. All models are trained with size 640×640 .

Model	AP ₅₀ ^{test}	AP _{50:95} ^{test}	#Param.
YOLOv8-n	78.6	57.5	3.0M
YOLOv8-s	81.6	61.6	11.1M
YOLOv8-m	83.7	65.3	25.9M
RREDet-n (\mathcal{C}_4)	84.1	65.2	2.9M
RREDet-s (\mathcal{C}_4)	86.3	67.6	10.5M
RREDet-m (\mathcal{C}_4)	87.4	70.3	25.7M

Table 4: Average Precise (AP) on the MSCOCO 2017 validation dataset. All models are trained with size 640×640 .

Model	AP ₅₀ ^{val}	AP _{50:95} ^{val}	#Param.
YOLOv5-s	56.8	37.4	7.2M
YOLOv6-n	53.1	37.5	4.7M
YOLOv7-tiny	55.2	37.4	6.2M
YOLOv8-n	52.6	37.3	3.2M
YOLOv9-n	53.1	38.3	2.0M
YOLOv10-n	-	38.5	2.3M
RREDet-n (\mathcal{C}_4)	55.2	40.2	3.1M

Conclusion

In this paper, we delve into the realm of rotational equivariant networks employed for modeling natural datasets, showcasing their superior performance in leveraging 2D or 3D rotation groups. Despite their advancements, existing rotational equivariant networks operate under the assumption of a strict uniform rotational symmetry prevalent across all features. However, the reality of natural datasets unveils a different story, where data seldom adheres to strict rotational symmetry but rather aligns with a relaxed rotational symmetry pattern, characterized by rotational Symmetry-Breaking. This inability to effectively accommodate rotational Symmetry-Breaking scenarios, particularly within natural datasets, necessitates a novel approach. To tackle this challenge, we introduce a simple yet powerful method involving a collection of adaptable G -Biases. Utilizing this innovative mechanism, we put forth the concept of **Relaxed Rotational Equivariant Convolution** (RREConv), tailored to address the nuances of relaxed rotational symmetry. Building upon our RREConv framework, we present RRENet, designed for classification tasks, and RREDet, optimized for 2D object detection missions. Through rigorous experimentation, our results unequivocally demonstrate the efficacy of our approach when applied to vision tasks involving natural datasets. Exploring symmetry breaking with rotational equivariance, both within the realms of 2D and 3D fields represents a compelling avenue for future research. We firmly believe that incorporating this relaxation principle into models improves their ability to accurately represent symmetry-breaking phenomena in real-world contexts.

References

Barone, M.; and Theophilou, A. 2008. Symmetry and symmetry breaking in modern physics. In *Journal of Physics: Conference Series*, volume 104, 012037. IOP Publishing.

Bogatskiy, A.; Ganguly, S.; Kipf, T.; Kondor, R.; Miller, D. W.; Murnane, D.; Offermann, J. T.; Pettee, M.; Shahan, P.; Shimmin, C.; and Thais, S. 2022. Symmetry Group Equivariant Architectures for Physics. *arXiv:2203.06153*.

Chidester, B.; Do, M. N.; and Ma, J. 2018. Rotation Equivariance and Invariance in Convolutional Neural Networks. *arXiv:1805.12301*.

Cohen, T. S.; and Welling, M. 2016a. Group Equivariant Convolutional Networks. *arXiv:1602.07576*.

Cohen, T. S.; and Welling, M. 2016b. Steerable CNNs. *arXiv:1612.08498*.

Desai, K.; Nachman, B.; and Thaler, J. 2022. Symmetry discovery with deep learning. *Physical Review D*, 105(9): 096031.

Dieleman, S.; De Fauw, J.; and Kavukcuoglu, K. 2016. Exploiting cyclic symmetry in convolutional neural networks. In *International conference on machine learning*, 1889–1898. PMLR.

Esteves, C. 2020. Theoretical aspects of group equivariant neural networks. *arXiv preprint arXiv:2004.05154*.

Fuchs, F. B.; Worrall, D. E.; Fischer, V.; and Welling, M. 2020. SE(3)-Transformers: 3D Roto-Translation Equivariant Attention Networks. *arXiv:2006.10503*.

Ghosh, S. K.; Biswas, P. K.; Xu, C.; Li, B.; Zhao, J. Z.; Hillier, A. D.; and Xu, X. 2022. Time-reversal symmetry breaking superconductivity in three-dimensional Dirac semimetallic silicides. *Physical Review Research*, 4(1).

Han, J.; Ding, J.; Xue, N.; and Xia, G.-S. 2021. ReDet: A Rotation-equivariant Detector for Aerial Object Detection. *arXiv:2103.07733*.

He, K.; Zhang, X.; Ren, S.; and Sun, J. 2014. *Spatial Pyramid Pooling in Deep Convolutional Networks for Visual Recognition*, 346–361. Springer International Publishing. ISBN 9783319105789.

He, K.; Zhang, X.; Ren, S.; and Sun, J. 2016. Deep residual learning for image recognition. In *Proceedings of the IEEE conference on computer vision and pattern recognition*, 770–778.

He, L.; Chen, Y.; Dong, Y.; Wang, Y.; Lin, Z.; et al. 2021. Efficient equivariant network. *Advances in Neural Information Processing Systems*, 34: 5290–5302.

Kaba, S.-O.; Mondal, A. K.; Zhang, Y.; Bengio, Y.; and Ravanbakhsh, S. 2023. Equivariance with Learned Canonicalization Functions. *arXiv:2211.06489*.

Kaba, S.-O.; and Ravanbakhsh, S. 2024. Symmetry Breaking and Equivariant Neural Networks. *arXiv:2312.09016*.

Kavukcuoglu, K.; Ranzato, M.; Fergus, R.; and LeCun, Y. 2009. Learning invariant features through topographic filter maps. In *2009 ieee conference on computer vision and pattern recognition*, 1605–1612. IEEE.

Kondor, R.; and Trivedi, S. 2018. On the Generalization of Equivariance and Convolution in Neural Networks to the Action of Compact Groups. *arXiv:1802.03690*.

Li, J.; Yang, Z.; Liu, H.; and Cai, D. 2018. Deep Rotation Equivariant Network. *arXiv:1705.08623*.

Li, Z.; Nagano, L.; and Terashi, K. 2024. Enforcing exact permutation and rotational symmetries in the application of quantum neural network on point cloud datasets. *arXiv preprint arXiv:2405.11150*.

Liu, H.; Yang, J.; Li, Z.; Li, K.; Zheng, J.; Wang, X.; Tang, X.; Chen, M.; You, X.; and Wei, X. 2024. ProEqBEV: Product Group Equivariant BEV Network for 3D Object Detection in Road Scenes of Autonomous Driving.

Marcos, D.; Volpi, M.; Komodakis, N.; and Tuia, D. 2017. Rotation Equivariant Vector Field Networks. In *2017 IEEE International Conference on Computer Vision (ICCV)*. IEEE.

Marcos, D.; Volpi, M.; and Tuia, D. 2016. Learning rotation invariant convolutional filters for texture classification. In *2016 23rd International Conference on Pattern Recognition (ICPR)*, 2012–2017. IEEE.

Müller, P.; Golkov, V.; Tomassini, V.; and Cremers, D. 2021. Rotation-Equivariant Deep Learning for Diffusion MRI. *arXiv:2102.06942*.

Ravanbakhsh, S.; Schneider, J.; and Poczos, B. 2017. Equivariance through parameter-sharing. In *International conference on machine learning*, 2892–2901. PMLR.

Romero, D. W.; and Lohit, S. 2023. Learning Partial Equivariances from Data. *arXiv:2110.10211*.

Seo, A.; Kim, B.; Kwak, S.; and Cho, M. 2022. Reflection and Rotation Symmetry Detection via Equivariant Learning. *arXiv:2203.16787*.

van der Ouderaa, T. F. A.; Romero, D. W.; and van der Wilk, M. 2022. Relaxing Equivariance Constraints with Non-stationary Continuous Filters. *arXiv:2204.07178*.

Veeling, B. S.; Linmans, J.; Winkens, J.; Cohen, T.; and Welling, M. 2018. Rotation Equivariant CNNs for Digital Pathology. *arXiv:1806.03962*.

Vernizzi, G.; and Wheater, J. F. 2002. Rotational symmetry breaking in multimatrix models. *Physical Review D*, 66(8): 085024.

Wang, R.; Hofgard, E.; Gao, H.; Walters, R.; and Smidt, T. E. 2024. Discovering Symmetry Breaking in Physical Systems with Relaxed Group Convolution. *arXiv:2310.02299*.

Wang, R.; Walters, R.; and Yu, R. 2022. Approximately equivariant networks for imperfectly symmetric dynamics. In *International Conference on Machine Learning*, 23078–23091. PMLR.

Wang, X.; Lei, J.; Lan, H.; Al-Jawari, A.; and Wei, X. 2023. DuEqNet: Dual-Equivariance Network in Outdoor 3D Object Detection for Autonomous Driving. *arXiv:2302.13577*.

Weiler, M.; and Cesa, G. 2021. General $E(2)$ -Equivariant Steerable CNNs. *arXiv:1911.08251*.

Weiler, M.; Geiger, M.; Welling, M.; Boomsma, W.; and Cohen, T. 2018. 3D Steerable CNNs: Learning Rotationally Equivariant Features in Volumetric Data. *arXiv:1807.02547*.

Wu, F.; Hu, P.; and Kong, D. 2015. Flip-rotate-pooling convolution and split dropout on convolution neural networks for image classification. *arXiv preprint arXiv:1507.08754*.

Zhu, K.; Zhang, X.; Chen, G.; Li, X.; Cai, P.; Liao, P.; and Wang, T. 2022. Multi-Oriented Rotation-Equivariant Network for Object Detection on Remote Sensing Images. *IEEE Geoscience and Remote Sensing Letters*, 19: 1–5.